Journal of Alloys and Compounds 521 (2012) 163–173

Contents lists available at SciVerse ScienceDirect

Journal of Alloys and Compounds

journal homepage: www.elsevier.com/locate/jallcom

Room-temperature MBE deposition, thermoelectric properties, and advanced structural characterization of binary Bi_2Te_3 and Sb_2Te_3 thin films

N. Peranio[a,*], M. Winkler[b], D. Bessas[c,d], Z. Aabdin[a], J. König[b], H. Böttner[b], R.P. Hermann[c,d], O. Eibl[a]

[a] Institut für Angewandte Physik, Eberhard Karls Universität Tübingen, Auf der Morgenstelle 10, D-72076 Tübingen, Germany
[b] Fraunhofer Institut Physikalische Messtechnik, Heidenhofstrasse 8, D-79110 Freiburg, Germany
[c] Jülich Centre for Neutron Science JCNS und Peter Grünberg Institut PGI, JARA-FIT, Forschungszentrum Jülich GmbH, D-52425 Jülich, Germany
[d] Faculté des Sciences, Université de Liège, B-4000, Liège, Belgium

ARTICLE INFO

Article history:
Received 3 December 2011
Received in revised form 16 January 2012
Accepted 18 January 2012
Available online 28 January 2012

Keywords:
Thermoelectric materials
Vapor deposition
X-ray diffraction
Transmission electron microscopy
Microstructure
Composition fluctuations

ABSTRACT

Sb_2Te_3 and Bi_2Te_3 thin films were grown at room temperature on SiO_2 and BaF_2 substrates using molecular beam epitaxy. A layer-by-layer growth was achieved such that metallic layers of the elements with 0.2 nm thickness were deposited. The layer structure in the as-deposited films was confirmed by X-ray diffraction and was seen more clearly in Sb_2Te_3 thin films. Subsequent annealing was done at 250 °C for 2 h and produced the Sb_2Te_3 and Bi_2Te_3 crystal structure as confirmed by high-energy X-ray diffraction. This preparation process is referred to as nano-alloying and it was demonstrated to yield single-phase thin films of these compounds. In the thin films a significant texture could be identified with the crystal *c* axis being almost parallel to the growth direction for Sb_2Te_3 and tilted by about 30° for Bi_2Te_3 thin films. In-plane transport properties were measured for the annealed films at room temperature. Both films yielded a charge carrier density of about 2.6×10^{19} cm^{-3}. The Sb_2Te_3 films were *p*-type, had a thermopower of +130 μV K^{-1}, and surprisingly high mobilities of 402 cm^2 V^{-1} s^{-1}. The Bi_2Te_3 films were *n*-type, showed a thermopower of −153 μV K^{-1}, and yielded significantly smaller mobilities of 80 cm^2 V^{-1} s^{-1}. The chemical composition and microstructure of the films were investigated by transmission electron microscopy (TEM) on cross sections of the thin films. The grain sizes were about 500 nm for the Sb_2Te_3 and 250 nm for the Bi_2Te_3 films. In the Bi_2Te_3 thin film, energy-filtered TEM allowed to image a Bi-rich grain boundary phase, several nanometers thick. This secondary phase explains the poor mobilities of the Bi_2Te_3 thin film. With these results the high potential of the nano-alloying deposition technique for growing films with a more complex layer architecture is demonstrated.

1. Introduction

For thermoelectric application at room temperature, Bi_2Te_3 based bulk materials are the best choice due to their high thermoelectric figure of merit $ZT = (S^2\sigma/\lambda)T \approx 1$ at $T = 300$ K, which is calculated from the thermopower ($S \approx \pm 200$ μV K^{-1}), the electrical conductivity ($\sigma \approx 1000$ S cm^{-1}), and the thermal conductivity ($\lambda \approx 1.5$ W m^{-1} K^{-1}) [1]. In bulk materials an increase of *ZT* beyond 1 was not achieved for several decades since the transport properties depend on each other, being given by fundamental parameters of the electron and phonon system. In their pioneering work Hicks and Dresselhaus [2] predicted a *ZT* enhancement in low-dimensional system due to quantum confinement and lattice phonon scattering. Venkatasubramanian et al. [3] fabricated hole-conducting Bi_2Te_3/Sb_2Te_3 and electron-conducting $Bi_2Te_3/Bi_2(Te_{0.94}Se_{0.06})_3$ superlattice structures which were grown on GaAs substrates by metalorganic chemical vapor deposition (MOCVD), showing a *ZT* of 2.4 and 1.7, respectively. In a previous work, electron-conducting Bi_2Te_3 thin films and $Bi_2Te_3/Bi_2(Te_{0.88}Se_{0.12})_3$ superlattices were epitaxially grown by molecular beam epitaxy (MBE) on BaF_2 substrates, yielding *ZT* values of 0.4–0.8 [4,5]. In the last decade the outstanding *ZT* values as obtained in thin films by Venkatasubramanian et al. could not be reproduced by any other group [6–13].

A major challenge of epitaxial MBE growth is stoichiometry control, since the sticking coefficient of Te is smaller than 0.6 at substrate temperatures beyond 300 °C [14]. In this work, binary Sb_2Te_3 and Bi_2Te_3 thin films were grown by nano-alloying which allows to overcome the problem of stoichiometry control [15]. Nano-alloying comprises alternate deposition of elemental layers at room temperature and subsequent annealing of the stacks for phase formation. Similar growth techniques were applied by Johnson [16] and Taylor et al. [17]. Chemical compositions of the films were monitored by high-accuracy energy-dispersive X-ray spectroscopy (EDX) in scanning and transmission electron microscopy (SEM

* Corresponding author. Tel.: +49 7071 29 76331; fax: +49 7071 29 5093.
E-mail address: nicola.peranio@uni-tuebingen.de (N. Peranio).

0925-8388/$ – see front matter © 2012 Elsevier B.V. All rights reserved.
doi:10.1016/j.jallcom.2012.01.108

Table 1
Structure and MBE growth parameters of as-grown and annealed Bi_2Te_3 and Sb_2Te_3 thin films. Values given without (in) parenthesis correspond to films deposited on BaF_2 (SiO_2) substrates.

Sample ID	Thin film	Annealing	Total film thickness (nm)
BT-B1 (BT-S1)	Bi_2Te_3	As-grown	1290 (1130)
BT-B2 (BT-S2)	Bi_2Te_3	250 °C for 2 h	1290 (1170)
ST-B1 (ST-S1)	Sb_2Te_3	As-grown	1150 (1150)
ST-B2 (ST-S2)	Sb_2Te_3	250 °C for 2 h	1140 (1110)

About 1000 quintuples stacks with the sequence Te–M–Te–M–Te (M = Bi or Sb) with elemental layer thicknesses of 0.2 nm were grown at room temperature on {1 1 1}-BaF_2 or on SiO_2 substrates.

and TEM) instruments; *e.g.*, for EDX in the TEM instrument Cliff-Lorimer *k*-factors were used which were calibrated on $Bi_2(Te,Se)_3$ and $(Bi,Sb)_2Te_3$ bulk materials [18,19].

For understanding transport properties and limitations for *ZT* enhancement, detailed analyses of the structure, texture, and chemical composition are required. Bi_2Te_3 based materials have a layered crystal structure and highly anisotropic transport properties [1]. Therefore, the texture of the films was investigated in detail by high-energy X-ray diffraction (XRD) in transmission and grazing incidence and by selected area electron diffraction (SAED) in the TEM. In epitaxial Bi_2Te_3 thin films and superlattices [4] it was shown that thermal conductivity was reduced due to phonon scattering on various structural defects, *i.e.*, grain boundaries/surfaces, dislocations, superlattice interfaces, and a structural modulation with a wavelength of 10 nm. However, charge carrier mobility was reduced as well, which inhibited a *ZT* enhancement in epitaxial thin films. For nano-alloyed thin films presented here, the charge carrier mobilities and their dependence on microstructure will be a main topic.

2. Experimental

2.1. Synthesis by nano-alloying and transport measurements

Bi_2Te_3 and Sb_2Te_3 have a rhombohedral layered structure with space group $R\bar{3}m$ and pseudo-hexagonal lattice parameters $a = 0.4386$ nm and $c = 3.0497$ nm for Bi_2Te_3 [20]. In this work, the pseudo-hexagonal notation was used for indexing of X-ray and electron diffraction patterns. For thin film growth by MBE, {1 1 1}-oriented single crystalline BaF_2 or commercial Si wafers with 100-nm amorphous SiO_2 on top were used as substrate materials. Barium fluoride has a face centered cubic structure with space group $Fm\bar{3}m$ and lattice parameter $a = 0.620$ nm [21].

Nominally stoichiometric Bi_2Te_3 and Sb_2Te_3 thin films were grown by MBE according to the two-step nano-alloying approach [15]: (i) the films were grown at room temperature in a EPI930 MBE [22] system by alternate deposition of elemental layers with sequence Te–M–Te–M–Te (M = Sb or Bi), each layer had a nominal thickness of 0.2 nm [23,24]. This particular deposition pattern was selected since it closely corresponds to the layered structure of Bi_2Te_3 and Sb_2Te_3. The total thickness of the films was about 1 μm (Table 1). The total growth rates were 0.33 μm/h for Sb_2Te_3 and 0.43 μm/h for Bi_2Te_3. The chemical elements were evaporated from standard thermal effusion cells. (ii) Post-annealing was conducted at 250 °C for 2 h. The isothermal annealing was done in an annealing assembly developed by Fraunhofer IPM. A closed ampoule evacuated to 10^{-6} mbar was used with additional Te as source material to avoid Te loss of the samples during annealing. The annealing assembly containing the ampoule was kept under nitrogen atmosphere.

Within a larger research effort series of Sb_2Te_3 and Bi_2Te_3, thin films were prepared for which the Te content was varied by varying the shutter opening time during the MBE deposition. For Sb_2Te_3 the Te mole fraction was varied between 56.5 at.% and 61.7 at.% and for Bi_2Te_3 between 52.3 at.% and 61.5 at.%. Thermoelectric data were measured for all samples of the series. Samples with the highest thermopower were selected for the structural characterization, as presented here.

The in-plane transport coefficients of the films were measured at room temperature. The electrical conductivity σ, the charge carrier mobility μ, and the charge carrier density n were measured by Hall-effect measurements using the van der Pauw method [23]. The thermopower S was measured by a calibrated setup using a Ni reference [23].

2.2. Analysis of texture, nanostructure, and chemical composition

The roughness of the elemental layers in as-deposited and annealed films grown on BaF_2 substrates (samples BT-B1, BT-B2, ST-B1, and ST-B2) were characterized with a Bruker AXS D8 ADVANCED reflectometer in $\theta - 2\theta$ Bragg-Brentano geometry using a Göbel mirror monochromator providing Cu K_α radiation.

Synchrotron radiation diffraction was carried out on annealed thin films grown on BaF_2 substrates (samples BT-B2 and ST-B2) at the 6-ID-D high-energy station, APS, Chicago, in order to determine lattice parameters, epitaxial relations, and texture. The synchrotron radiation energy was set to 87.3045 keV yielding a wavelength of 0.142013 (5) Å; the detector position was refined using NIST640c standard Si powder. This wavelength was used in order to be below the Bi K_α absorption edge. The data was collected with a 2000 × 2000 pixel amorphous Si detector. The beam size was defined to 50 μm × 50 μm. The samples were analyzed (i) in transmission with the beam parallel to the surface normal, *i.e.*, parallel to the {1 1 1} reciprocal direction of the BaF_2 substrate, and (ii) in grazing incidence geometry with the beam parallel to the ⟨2 1 1⟩direction of the BaF_2 substrate.

Cross-sectional specimens were prepared for analysis in a TEM. The TEM specimens were prepared from annealed samples grown on SiO_2//Si substrates (samples BT-S2 and ST-S2). For cross sectional TEM specimen preparation, a Si dummy was glued on top of the film. The conventional thinning procedure was applied to the Si//Bi_2Te_3//SiO_2//Si composites. This procedure included mechanical grinding and polishing down to a thickness of 25 μm, followed by Ar^+-ion milling at 3–4 kV. TEM specimens were 3 mm in diameter and were mounted on a 100 μm thick Al ring.

A Zeiss 912 Ω TEM with a LaB_6 gun was used, operated at 120 kV, having a point resolution of 0.37 nm and an energy resolution of 1 eV. Crystallinity and grain orientation were analyzed by electron diffraction. For this, a SAED aperture was used selecting specimen regions for diffraction with a diameter of 750 nm. High-resolution images of grains with strongly excited {0 0 *l*} Bragg reflections were acquired. The size of the grains and the dislocation densities were determined by acquisition of bright- and dark-field images of grains in two-beam diffraction conditions. Particularly, with strongly excited {0 1 5} reflections a structural modulation with a wavelength of 10 nm [natural nanostructures (nns)] can be observed [4,25].

The chemical compositions of the films were determined by EDX spectroscopy in (i) a Hitachi S4700 SEM with an EDAX EDX system and an accuracy of 0.5 at.% using bulk Bi_2Te_3 and Sb_2Te_3 calibration standards and (ii) in the TEM using bulk calibrated Cliff-Lorimer *k*-factors for quantitative chemical analysis [19,26]. Chemical analyses by EDX in the SEM and TEM were in agreement due to calibration as will be shown. In a previous study on Bi_2Te_3 based bulk materials, a high-accuracy quantitative chemical analysis by EDX in the TEM instrument was established [19]. EDX spectra were acquired with a spot size of 32 nm and an acquisition time of 300 s. The Cliff-Lorimer *k*-factors were calibrated by combined EDX spectroscopy in the TEM and electron probe microanalyses (EPMA) [19]. The integrated counts N under the Bi L and Te L X-ray lines were larger than 15 000 yielding a minimum statistical error of $\sigma_N/N = 0.8\%$ (Poisson statistics) for the determination of the local mole fractions.

Finally, for electron energy-loss spectroscopy (EELS) and phase mapping by energy-filtered TEM (EFTEM) the microscope is equipped with an OMEGA® energy filter, the energy resolution was limited to 1.0–1.3 eV. Low-loss EEL spectra were acquired with a spot size of 10 nm. The position of the plasmon peak was determined with an accuracy of 0.2 eV. For phase mapping, the spectrometer exit aperture with a slit width of 5 eV was inserted and three EFTEM images were acquired and were superimposed to RGB images: two EFTEM images (red and blue) were acquired for 17 eV energy loss and one EFTEM image (green) for 25 eV energy loss, the selected energy losses being close to the plasmon energy and the Bi $O_{4,5}$ ionization edge, respectively.

3. Results

3.1. Sb_2Te_3 thin films

3.1.1. Transport properties before and after annealing

The room-temperature in-plane transport coefficients of as-grown and annealed Sb_2Te_3 films are summarized in Table 2, including the Te content determined by EDX in the SEM. All Sb_2Te_3 thin films were *p*-type, which is the usual case for this compound [1]. Films deposited on BaF_2 and SiO_2 substrates yielded similar transport properties (Table 2).

In the as-grown state, a low charge carrier mobility of $\mu \approx 40\,cm^2\ V^{-1}\ s^{-1}$ and thereby a small power factor of $S^2\sigma < 3\ \mu W\,cm^{-1}\,K^{-2}$ were found. On the other hand, a small charge carrier density of $p = 2.4 \times 10^{19}\ cm^{-3}$ and consequently a large thermopower of $S \approx 120\ \mu V\,K^{-1}$ were obtained.

After annealing, charge carrier density and thermopower slightly increased by less than 10%, whereas the charge carrier mobility and thereby the power factor significantly increased by a factor of ten. Finally, heat conductivity was measured in cross-plane direction and yielded a promising low value of $1.6\ W\,m^{-1}\,K^{-1}$, details will be presented elsewhere.

Table 2
Te content and in-plane transport properties of Sb_2Te_3 and Bi_2Te_3 thin films measured at room temperature: carrier density n, carrier mobility μ, electrical conductivity σ, thermopower S, power factor $S^2\,\sigma$.

Sample	Te (at. %)	n (cm^{-3})	μ ($cm^2\,V^{-1}\,s^{-1}$)	σ ($\Omega^{-1}\,cm^{-1}$)	S ($\mu V\,K^{-1}$)	$S^2\,\sigma$ ($\mu W\,cm^{-1}\,K^{-2}$)
As-grown						
BT-B1	59.3	-1.9×10^{21}	1.6	469	−52	1.3
BT-S1	58.3	-1.0×10^{21}	2.8	451	−53	1.3
ST-B1	60.5	2.4×10^{19}	43	164	119	2.3
ST-S1	60.5	2.4×10^{19}	42	162	127	2.6
Annealed at 250 °C for 2 h						
BT-B2	59.4	-2.7×10^{19}	61	270	−182	9
BT-S2	59.1	-2.7×10^{19}	80	338	−153	8
ST-B2	61.1	2.8×10^{19}	433	1929	125	30
ST-S2	61.0	2.6×10^{19}	402	1696	130	29

Carrier density values with a negative sign indicate electron conduction; a positive value indicates hole conduction. The Te content was determined by EDX in the SEM.

3.1.2. XRD on as-grown and annealed thin films

The $\theta-2\theta$ diffractograms of the as-grown and annealed Sb_2Te_3 films deposited on BaF_2 substrates are shown in Fig. 1. Minor variations in the single-crystal BaF_2 peak-tails for the different samples are due to small variations in the monochromator alignment, affecting the suppression of radiations others than K_α. For {0,0,15} film reflections, the peak positions, the full widths at half maximum (FWHM), and the correlation lengths in real space corresponding to the FWHM were determined from a fit with a Lorentzian profile, see Table 3. The FWHM of a BaF_2 single-crystal peak was also determined, which indicates the resolution function.

The as-deposited films only exhibited $\{0\,0\,l\}$ reflections of the Sb_2Te_3 structure. After annealing, $\{0\,0\,l\}$ as well as various $\{h\,k\,l\}$ reflections of the Sb_2Te_3 structure were observed. The $\{0\,0\,l\}$ reflections of the as-deposited samples were broader by an order of magnitude than the equivalent reflections in the annealed samples (Table 3). Correspondingly, the correlation lengths were by an order of magnitude smaller for the as-grown film as compared to the annealed film. Also, the $\{0\,0\,l\}$ reflections were shifted by 1% after annealing as compared to the as-grown state. In summary, the annealing at 250 °C significantly improved the crystalline quality of the Sb_2Te_3 films at the expense of texturing.

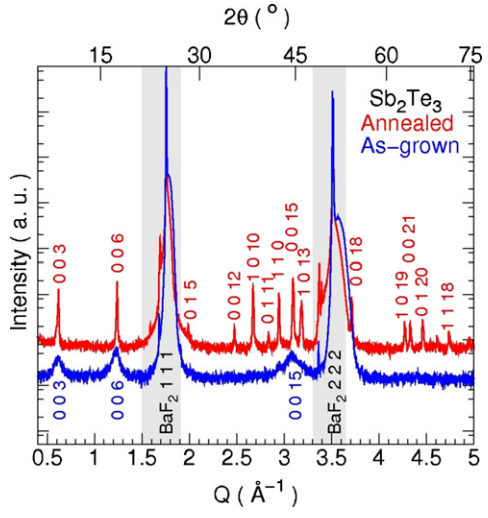

Fig. 1. (color online) XRD results obtained on as-grown (blue) (For interpretation of the references to color in this figure legend, the reader is referred to the web version of the article.) and annealed (red) Sb_2Te_3 thin films deposited on a BaF_2 substrate (samples ST-B1 and ST-B2). The diffractograms were acquired in $\theta-2\theta$ geometry with the scattering vector perpendicular to the {1 1 1} BaF_2 substrate. Reflections of the Sb_2Te_3 films are indexed in red and in blue, reflections of the substrate are marked in grey zones. Note the logarithmic intensity scale and that the curves were logarithmically shifted for clarity.

3.1.3. TEM on annealed thin films

The TEM bright-field images and an electron diffraction pattern as shown in Fig. 2 were obtained in a cross section of an annealed Sb_2Te_3 thin film deposited on a SiO_2 substrate. The substrate was almost completely removed by ion milling, only some fractions of the SiO_2 buffer layer remained (Fig. 2(a)). The total film thickness was determined as 1.05 μm. The roughness of the thin film-substrate interface was less than 10 nm whereas the surface showed a roughness of about 40 nm. Within the film, grains with diameters between 350 nm and 650 nm were observed, see Fig. 2(a) and (b). Two adjacent grains separated by a large-angle grain boundary are shown in more detail in diffraction contrast in Fig. 2(c). In both grains a fringe pattern appeared due to a structural modulation (nns) [25] with a wavelength between 5 and 12 nm. In Fig. 2(d) an electron diffraction pattern obtained on two grains located at the film–substrate interface (Fig. 2(b)) is shown. In both grains $\{0\,0\,l\}$ reflections were strongly excited. The grains enclosed an angle of 18° and their crystal c axes deviated by an angle of up to 37° from growth direction (Fig. 2(d)). Note that even for grains directly located at the substrate significant deviations from c orientation were observed. From the diffraction patterns the lattice parameters were determined yielding $a = 0.424$ nm and $c = 3.04$ nm. Finally, a radial intensity profile (Fig. 2(e)) was obtained from the diffraction pattern (Fig. 2(d)), being in agreement with XRD results (Fig. 1).

An EDX spectrum and a low-loss EEL spectrum are shown in Fig. 3(a) and (b), respectively. Eight EDX spectra were acquired yielding a chemical composition of 40.3 at.% Sb and 59.7 at.% Te and a standard deviation of 0.6 at.%, the variations being mainly determined by counting statistics. EDX results obtained in the SEM (Table 2) and TEM were found to be in agreement within the experimental error. From the EEL spectrum shown in Fig. 3(b) a plasmon energy of 16.2 eV was determined. The position of the Sb $N_{4,5}$ and Te $N_{4,5}$ ionization edges were marked by arrows in Fig. 3(b). The Sb $N_{4,5}$ ionization edge is superimposed by the second plasmon peak.

3.2. Bi_2Te_3 thin films

3.2.1. Transport properties before and after annealing

The room-temperature in-plane transport coefficients of as-grown and annealed Bi_2Te_3 films are summarized in Table 2. The Bi_2Te_3 thin films of the series studied were n-type in both cases, for Bi excess as well as for Te excess. It was impossible to obtain hole-like conduction. From Bi_2Te_3 bulk material the charge carriers were expected to be holes for stoichiometric material and electrons in case of Te excess [1]. The films grown on BaF_2 substrates (samples BT-B1 and BT-B2) and on SiO_2 substrates (samples BT-S1 and BT-S2) as shown in Table 2 correspond to two different runs and represent two typical examples of nano-alloyed Bi_2Te_3 films synthesized for this work. The composition of the samples varied

Table 3
XRD results obtained on as-grown and annealed Bi_2Te_3 and Sb_2Te_3 thin films deposited on BaF_2 substrates.

Sample	Peak	Peak position (Å^{-1})	FWHM (Å^{-1})	Correlation length (Å)
As-grown				
BT-B1	{0,0,15}	3.0932 (4)	0.022 (1)	290 (10)
ST-B1	{0,0,15}	3.0830 (10)	0.17 (1)	37 (2)
Annealed at 250 °C for 2 h				
BT-B2	{0,0,15}	3.0883 (1)	0.0178 (7)	350 (10)
ST-B2	{0,0,15}	3.0927 (1)	0.0121 (1)	519 (5)

Peak positions, full width at half maximum (FWHM), and correlation lengths were obtained from X-ray diffractograms in $\theta - 2\theta$ geometry after fitting with a Lorentzian profile. For comparison, BaF_2 yielded peaks with a FWHM of 0.006 (1) Å^{-1} and a correlation length larger than 1000 (200) Å.

slightly from run to run due to fluctuations of evaporation cell pressures during deposition. Usually, the desired element composition can be attained with a precision of about 0.5–1 at.%.

Similar to Sb_2Te_3, as-grown Bi_2Te_3 thin films yielded a small charge carrier mobility of $\mu < 3\,cm^2\,V^{-1}\,s^{-1}$ and thereby a small power factor of $S^2\sigma < 3\,\mu W\,cm^{-1}\,K^{-2}$. However, the as-deposited thin films showed pronounced metallic properties, *i.e.*, a large charge carrier density of $n = 1.0 \times 10^{21}\,cm^{-3}$ and thereby a small thermopower of $S = -53\,\mu V\,K^{-1}$.

After annealing, the charge carrier densities were reduced by two orders of magnitude to $2.7 \times 10^{19}\,cm^{-3}$ and the absolute thermopower significantly increased, *i.e.*, $|S| > 150\,\mu V\,K^{-1}$. The charge carrier mobilities increased to about $70\,cm^2\,V^{-1}\,s^{-1}$; however, this is a rather poor improvement as compared to $120\,cm^2\,V^{-1}\,s^{-1}$ determined in epitaxial Bi_2Te_3 thin films [4]. Thin films annealed for up to 72 h yielded an increase of charge carrier mobility up to $88\,cm^2\,V^{-1}\,s^{-1}$. In summary, after annealing Bi_2Te_3 thin films showed a small power factor of $S^2\sigma \approx 8\,\mu W\,cm^{-1}\,K^{-2}$ which can be attributed to a small charge carrier mobility. Finally, heat conductivity was measured in cross-plane direction and yielded a promising low value of $0.4\,W\,m^{-1}\,K^{-1}$, details will be presented elsewhere.

3.2.2. XRD on as-grown and annealed thin films

The diffractograms of a characteristic set of as-deposited and annealed Bi_2Te_3 films grown on BaF_2 substrates are shown in Fig. 4. The peak positions, the FWHM, and the correlation lengths are given in Table 3.

Both as-deposited and annealed thin films exhibited $\{0\,0\,l\}$ reflections as well as various $\{h\,k\,l\}$ reflections of the Bi_2Te_3 structure. The $\{0\,0\,l\}$ reflections found in as-deposited samples were 20% broader than the equivalent reflections observed in the annealed samples (Table 3). Correspondingly, correlation lengths were 20% smaller for the as-grown film as compared to the annealed film. The peak positions of the $\{0\,0\,l\}$ reflections were shifted by 0.1% after annealing.

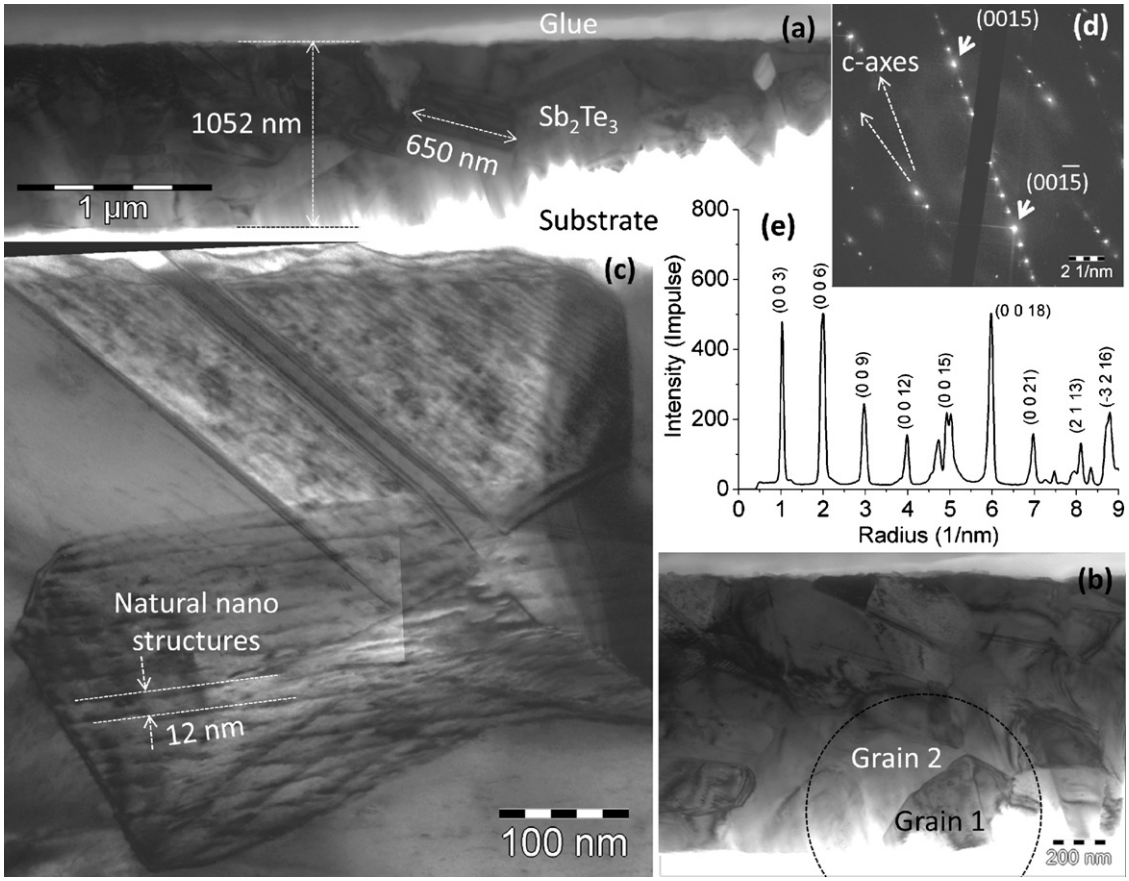

Fig. 2. TEM cross-section results obtained on the annealed Sb_2Te_3 thin film deposited on a SiO_2 substrate (sample ST-S2). In images (a)–(d) the growth direction points towards the top of the images. (a) Overview bright-field image. (b) Magnified bright-field image. (c) High magnification bright-field image of grain boundaries. (d) Selected area electron diffraction pattern of the encircled area in (b). (e) Normalized radial intensity profile obtained from the diffraction pattern.

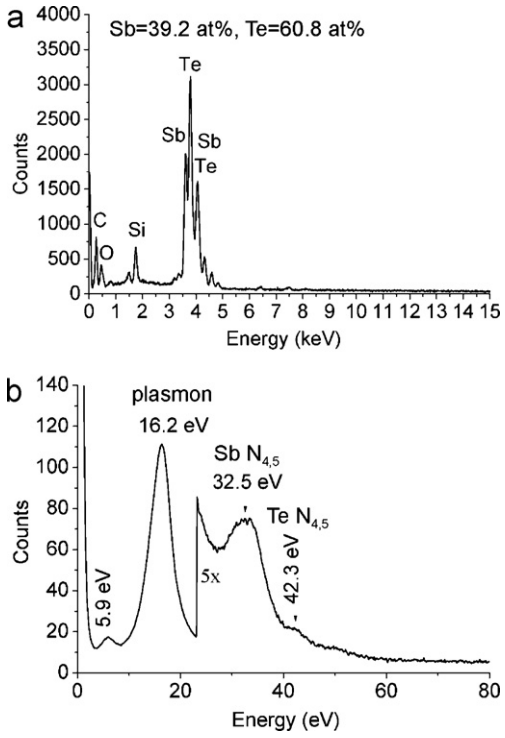

Fig. 3. TEM spectroscopy results obtained on the annealed Sb_2Te_3 thin film deposited on a SiO_2 substrate (sample ST-S2): (a) EDX spectrum and (b) low-loss EEL spectrum.

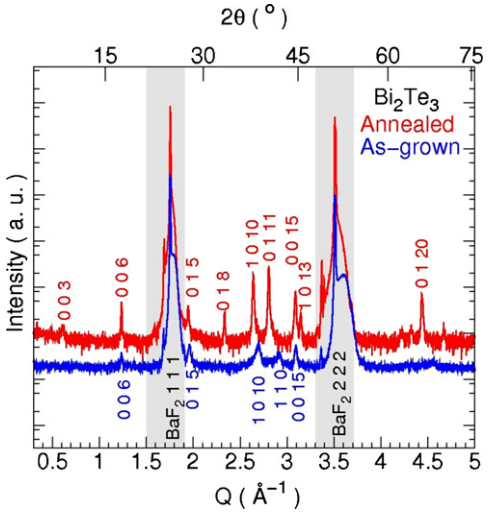

Fig. 4. (color online) XRD results obtained on as-grown (blue) and annealed (red) Bi_2Te_3 thin films deposited on a BaF_2 substrate (samples BT-B1 and BT-B2). The diffractograms were acquired in $\theta - 2\theta$ geometry with the scattering vector perpendicular to the {1 1 1} BaF_2 substrate. Reflections of the Bi_2Te_3 films are indexed in red and in blue, reflections of the substrate are marked in grey zones. Note the logarithmic intensity scale and that the curves were logarithmically shifted for clarity. (For interpretation of the references to color in this figure legend, the reader is referred to the web version of the article.)

For high-energy XRD using synchrotron radiation, diffraction patterns were acquired on the same sample in two different orientations: (i) in transmission geometry with the beam parallel to the {1 1 1} reciprocal direction of the BaF_2 substrate (Fig. 5(a)), and thus parallel to the growth direction, and (ii) in grazing incidence geometry with the beam perpendicular to the BaF_2 {1 1 1} and {0,2,−2} reciprocal directions (Fig. 6(a)). Note that the peaks of the BaF_2 substrate are seen due to substantial diffuse scattering rather than Bragg diffraction.

The diffraction patterns in Fig. 5(a) and Fig. 6(a) should be interpreted as follows: the radial distance from the center of the diffraction pattern corresponds to the scattering angle 2θ and the arc at a given radius corresponds to the azimuthal angle φ. The one dimensional diffractograms of the films (Fig. 5(c) and Fig. 6(b)), also referred to as radial intensity profiles, were obtained after masking out the substrate diffuse scattering and azimuthally integrating the remaining data.

All reflections could be indexed to the Bi_2Te_3 and BaF_2 structures. No extra reflections were found, indicating that no crystalline impurity phases were present. The lattice parameters of the thin films were calculated, see Table 4. The extracted values for Bi_2Te_3 and Sb_2Te_3 films (Sb_2Te_3 XRD patterns are shown here) agreed well with reference data obtained on polycrystalline samples [20,27].

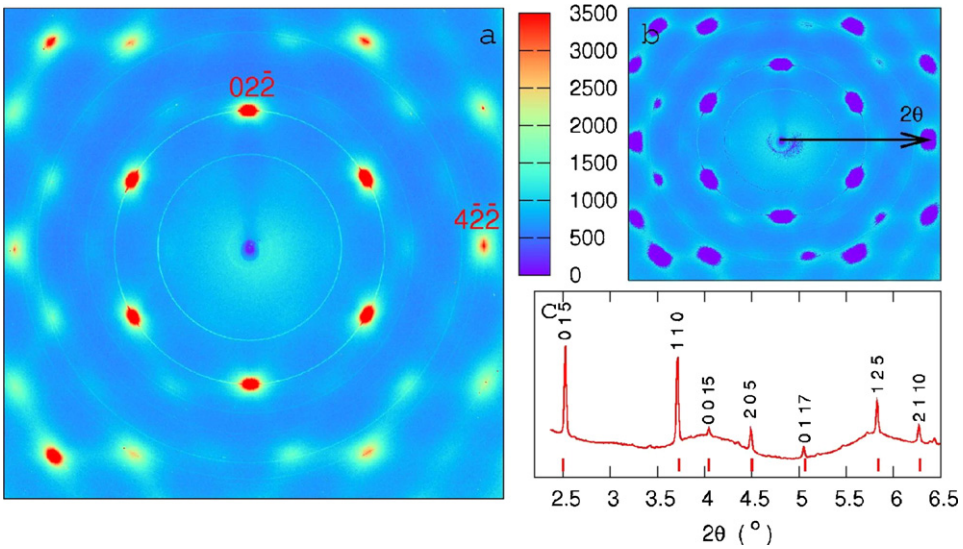

Fig. 5. (color online) High-energy XRD results obtained in transmission geometry on an annealed Bi_2Te_3 thin film deposited on a BaF_2 substrate (sample BT–B2). (a) Two dimensional diffraction pattern obtained for the beam parallel to the {1 1 1} reciprocal direction of the BaF_2 substrate. The single-crystal BaF_2 reflections are indexed in red. (b) The BaF_2 reflections were masked out as indicated in order to obtain (c) the one dimensional diffractogram of the film. (For interpretation of the references to color in this figure legend, the reader is referred to the web version of the article.)

Table 4
Lattice parameters of annealed Bi_2Te_3 and Sb_2Te_3 thin films deposited on BaF_2 substrates as determined by high-energy XRD.

Reference	a (nm)	c (nm)
Bi_2Te_3		
This work, sample BT-B2	0.4383 (1)	3.0413 (9)
Nakajima [20]	0.4386 (5)	3.0497 (20)
Sb_2Te_3		
This work, sample ST-B2	0.4265 (5)	3.0446 (9)
Anderson and Krause [27]	0.4264 (1)	3.0458 (7)

The diffraction patterns and diffractograms obtained on Bi_2Te_3 thin films in transmission (Fig. 5) and grazing incidence geometry (Fig. 6) markedly differed: (i) the {1,0,10} reflection was not observed in transmission geometry (Fig. 5(c)) but revealed strikingly high intensity in grazing incidence geometry (Fig. 6(b)). Also, in transmission geometry the intensity of the {1 1 0} reflection is significantly larger than that of the {0,0,15} reflection (Fig. 5(c)), in contrast to diffraction in grazing incidence geometry (Fig. 6(b)). (ii) For the thin film oriented in transmission geometry the intensities of the diffraction rings showed no azimuthal dependence (Fig. 5(a)), hence, there was no epitaxial relation between thin film and substrate. For the thin film oriented in grazing incidence a strong azimuthal dependence of the intensities of the diffraction rings was found; particularly, the {0,0,15} diffraction ring yielded peak maxima for $\varphi = 180^\circ \pm 30^\circ$ (Fig. 6(d)), where 180° corresponds to the BaF_2 {1 1 1} reciprocal direction (Fig. 6(a)). Hence, the c axis of the crystals was found to be inclined by 30° with respect to the growth direction.

3.2.3. TEM on annealed thin films

TEM bright-field and dark-field images and an electron diffraction pattern obtained in a cross section of an annealed Bi_2Te_3 thin film deposited on a SiO_2 substrate are shown in Fig. 7. The substrate and parts of the thin film were removed by ion milling (Fig. 7(a)). The film had a thickness of 1.18 μm, a roughness of less than 10 nm at the thin film/substrate interface, and a surface roughness of about 90 nm. Within the film, grains with diameters between 150 nm and 350 nm were observed, see Fig. 7(a) and Fig. 9(a). In Fig. 7(b) and (c) a TEM bright-field and a corresponding dark-field image of two adjacent grains labeled #1 and #2 are shown. The grains were separated by a large-angle grain boundary. Grain #2 revealed a structural modulation (nns) with a wavelength of 10 nm. In contrast to the Sb_2Te_3 thin films, the Bi_2Te_3 thin films revealed secondary phases at the grain boundaries, see below. Several grains contributed to the diffraction pattern shown in Fig. 7(d). The grains were found to be separated by large-angle grain boundaries and the c axis of the grains deviated by an angle of up to 39° from growth direction. From the diffraction patterns the lattice parameters were determined yielding $a = 0.450$ nm and $c = 3.10$ nm. Finally, a radial intensity profile (Fig. 7(e)) was obtained from the diffraction pattern (Fig. 7(d)), being in agreement with high-energy XRD results (Fig. 6(b)).

Spectroscopy was first applied to the Bi_2Te_3 matrix of the thin film, the analysis of the grain boundary phases will be shown below. The EDX and low-loss EEL spectra shown in Fig. 8(a) and (b), respectively, were acquired with the electron beam focused on the center of the grains. Six EDX spectra were acquired which revealed a chemical composition of 40.4 at.% Bi and 59.6 at.% Te and a standard deviation of 1.3 at.%, the variations being significantly larger than in the Sb_2Te_3 films and larger than the error from the counting statistics. A plasmon energy of 16.7 eV was determined and the position

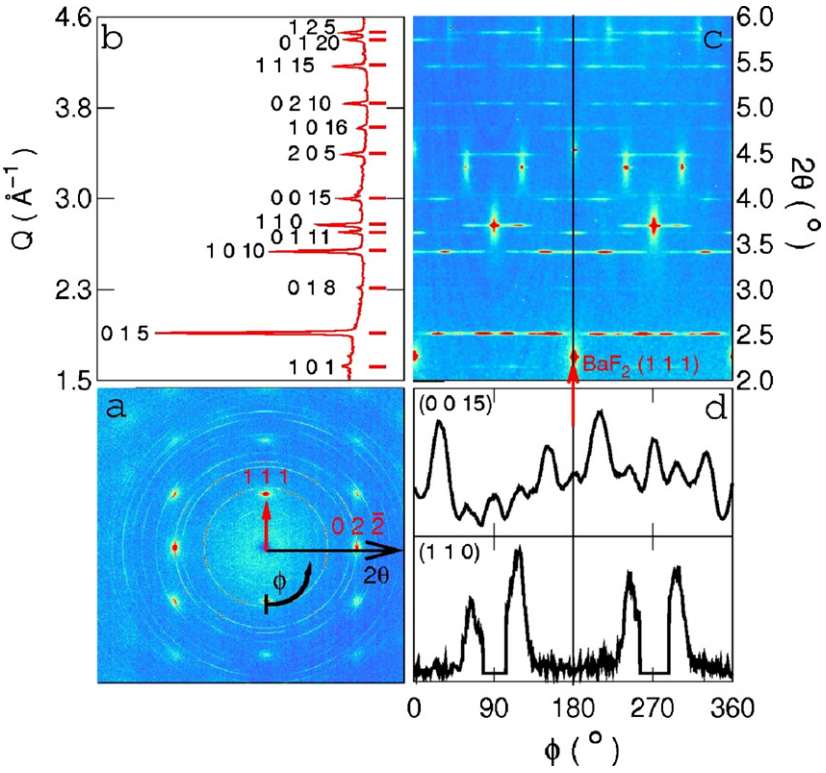

Fig. 6. (color online) High-energy XRD results obtained in grazing incidence geometry on annealed Bi_2Te_3 thin film deposited on a BaF_2 substrate (sample BT–B2). (a) Two dimensional diffraction pattern obtained for the beam oriented parallel to the substrate, *i.e.*, with the substrate in [2,−1,−1] pole orientation. The single-crystal reflections of the BaF_2 substrate are indexed in red. (b) Radial intensity profile of the film obtained from the two dimensional diffraction pattern, the BaF_2 reflections were masked out. (c) The diffraction data in (a) was transformed to azimuthal coordinates using the BaF_2 (−1,−1,−1) reciprocal direction as reference (*i.e.* $\phi = 0^\circ$). (d) Azimuthal dependence of the intensity of the Bi_2Te_3 {1,1,0} and {0,0,15} reflections. (For interpretation of the references to color in this figure legend, the reader is referred to the web version of the article.)

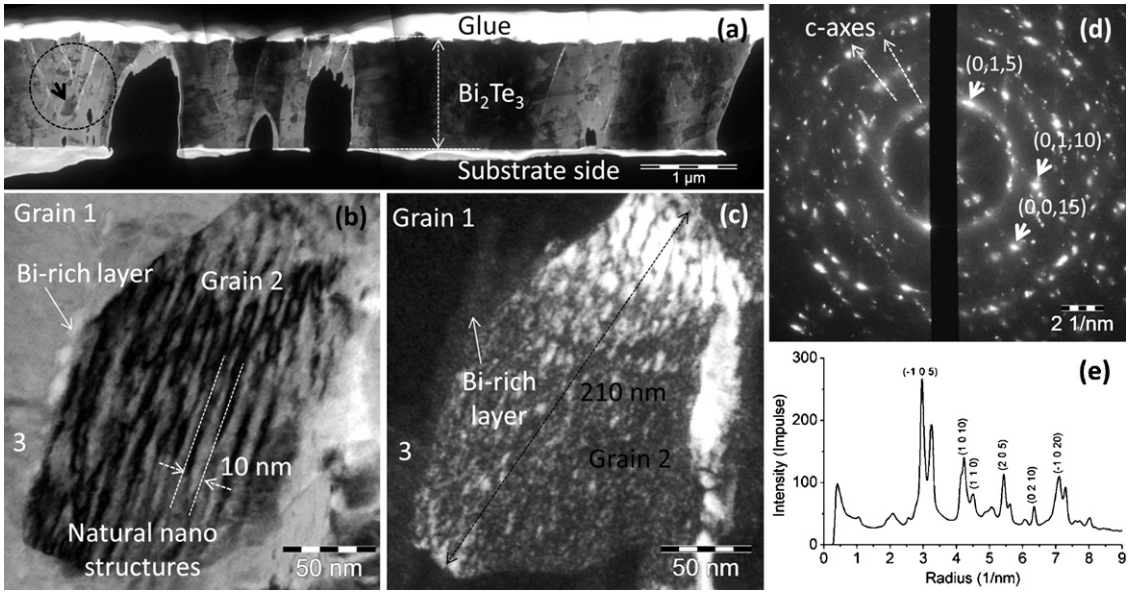

Fig. 7. TEM cross-section results obtained on the annealed Bi_2Te_3 thin film deposited on a SiO_2 substrate (sample BT-S2). In images (a)–(d) the growth direction points towards the top of the images. (a) Overview bright-field image. (b) High-magnification bright-field and (c) corresponding dark-field image of a grain. (d) Selected area electron diffraction pattern obtained on the encircled area in (a). (e) Normalized radial intensity profile obtained from the diffraction pattern.

of the Bi $O_{4,5}$ and Te $N_{4,5}$ ionization edges are marked by arrows in Fig. 8(b).

The grain boundary phases were analyzed in more detail by EDX and EEL spectroscopy and by EFTEM. In Fig. 9(a) and (b) a TEM bright-field image and a corresponding RGB map are shown, respectively. The RGB map was obtained by superposition of three energy-filtered images for energy-losses of 17, 25 (=Bi $O_{4,5}$), and 17 eV, respectively. As confirmed by EDX, in the RGB map green regions turned out to be Bi-rich grain boundary phases whereas the

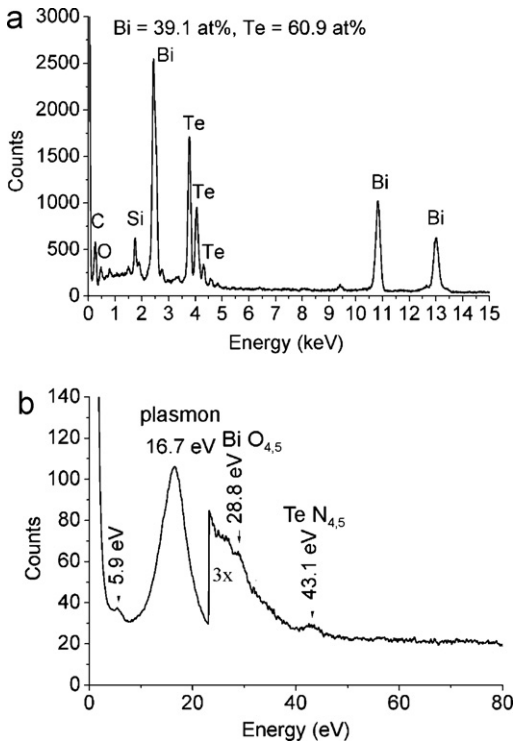

Fig. 8. TEM spectroscopy results obtained on the annealed Bi_2Te_3 thin film deposited on a SiO_2 substrate (sample BT-S2): (a) EDX spectrum and (b) low-loss EEL spectrum of the Bi_2Te_3 matrix.

Bi_2Te_3 matrix of the film is in purple (Fig. 9(b)). The Bi-rich grain boundary phases formed continuous layers extended in growth direction, with a thickness of about 10–20 nm, and separated by 150 nm from each other. Chemical analysis of the grain boundary phases by EDX (Fig. 9(c)) yielded a Bi mole fraction of up to 54 at.% and a significant Oxygen peak with a peak to background ratio, being by a factor of 7 larger in the grain boundary phases than in the matrix. In Bi-rich layers (Fig. 9(d)) the plasmon peak was shifted from an energy of 16.7–20.6 eV.

Finally, the high-resolution TEM images shown in Fig. 10(a) and (d) were obtained at two different regions of adjacent Bi_2Te_3 grains, labeled #1 and #2, and with a Bi-rich layer at the grain boundary (Fig. 10(a)). The grains were tilted by 70° with respect to each other. In both grains {0 0 3} lattice fringes with a lattice spacing of about 1 nm could be observed (Fig. 10(a) and (d)). Bright-field and dark-field TEM images were acquired at the grain boundary with a lower magnification, as shown in Fig. 10(b) and (c). Both grains revealed faceted grain boundaries with a wavelength of 15 nm and an amplitude of 9 nm (Fig. 10(d)). Some grains revealed dislocations (Fig. 10(e)), a small dislocation density of 1×10^6 cm^{-2} was obtained as compared to a dislocation density of 1×10^9 cm^{-2} found in bulk materials and thin films [4,25,28].

4. Discussion

4.1. As-deposited films: stoichiometry control and layer-by-layer growth

For MBE growth of Bi_2Te_3 and Sb_2Te_3 films substrate temperatures in the range of 225–350 °C are used (Table 5) [4–12]. In a previous study of epitaxially grown Bi_2Te_3 thin films an optimum substrate temperature of T_S = 290 °C and a flux ratio F_R = Te/Bi = 12/5 was found [4,5,22]. However, stoichiometry control is rather difficult due to the small sticking coefficient of tellurium at high substrate temperatures and the strong temperature dependence of the sticking coefficient. A sticking coefficient K_S(Te) = 0.6 was obtained for T_S = 310 °C and F_R = 2 [14]. As an alternative approach, room-temperature MBE together with a subsequent annealing step was found as a promising route [15,17] to obtain thin films with controlled stoichiometry as demonstrated in this work (Table 2).

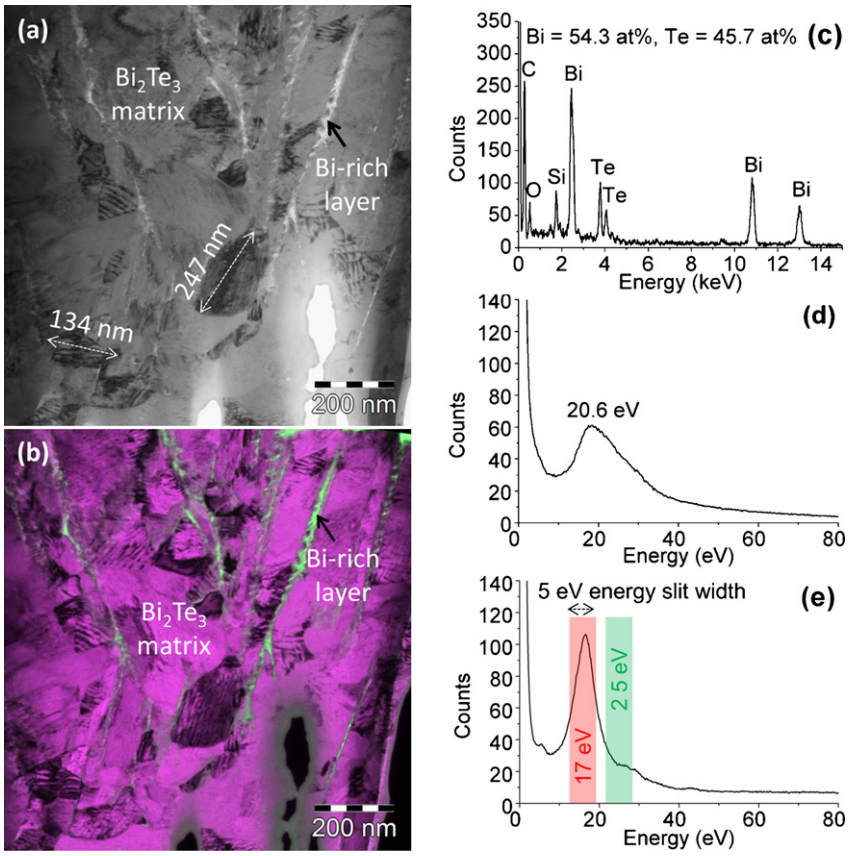

Fig. 9. (color online) TEM results obtained on Bi-rich layers in the annealed Bi_2Te_3 thin film deposited on a SiO_2 substrate (sample BT-S2). In images (a) and (b) the growth direction points towards the top of the images. (a) Bright-field image. (b) Superimposition of energy-filtered images (RGB map) yielding Bi-rich layers. (c) EDX spectrum of Bi-rich layer. (d) Low-loss EEL spectrum of Bi–rich layer. (e) Low-loss EEL spectra of the Bi_2Te_3 matrix together with the energy windows used for energy-filtered imaging.

As-deposited Sb_2Te_3 films yielded pronounced X-ray reflections with spacings only compatible with $\{0\,0\,l\}$ reflections of the Sb_2Te_3 structure. Particularly, the diffractogram (Fig. 1) of the as-grown film revealed fifth-order reflections, *i.e.*, {0,0,15}, which corresponded to layers with spacing of 0.204 nm (Table 3), being in agreement with the intended elemental layer thicknesses. This proved the high quality and accuracy of the room-temperature MBE deposition. Aside from the charge carrier mobility, the electronic

Table 5
Te content, charge carrier density n, thermopower S, charge carrier mobility μ, electrical conductivity σ, and power factor $S^2\,\sigma$ of nano-alloyed Sb_2Te_3 and Bi_2Te_3 thin films as compared to properties of thin films and bulk materials reported in the literature.

Sample	Growth method/Film thickness	Ref.	T_{max} (°C)	Te (at.%)	n (cm^{-3})	μ ($cm^2\,V^{-1}\,s^{-1}$)	σ ($\Omega^{-1}\,cm^{-1}$)	S ($\mu V\,K^{-1}$)	$S^2\,\sigma$ ($\mu W\,cm^{-1}\,K^{-2}$)
Sb_2Te_3									
Thin film[a]	Room-temperature MBE/1 μm, sample ST-S2	This work	250	61.0	2.6×10^{19}	402	1696	130	29
Thin film[b]	MOCVD/≈0.5 μm	[3]	225	60.0[d]	3.1×10^{19}	383	1901	201	77
Thin film[a]	Coevaporation/1 μm	[6]	230	60.0[d]	1.4×10^{19}	303	775	160	20
Bulk[c]	Bridgman	[38]	617	60.0	8.1×10^{19}	365	4762	79	30
Bi_2Te_3									
Thin film[a]	Room-temperature MBE/1 μm, sample BT-S2	This work	250	59.1	-2.7×10^{19}	80	338	−153	8
Thin film[a]	Room-temperature MBE/0.1 μm	[17]	250	60.0	-4.0×10^{19}	60	384	−170	11
Thin film[a]	Epitaxial MBE/1 μm	[4]	290	60.6	-3.3×10^{19}	120	670	−201	27
Thin film[a]	Coevaporation/1 μm	[6]	262	61.5[d]	-3.1×10^{19}	113	532	−208	23
Bulk[c]	Bridgman	[38]	585	60.0	0.5×10^{19}	465	377	277	29

Transport properties of nano-alloyed thin films were measured at room temperature. The temperature T_{max} is the maximum temperature the materials were exposed to during synthesis. Carrier density values with a negative sign indicate electron conduction; a positive value indicates hole conduction.

[a] Binary thin film. In-plane transport properties were determined.
[b] Sb_2Te_3/Bi_2Te_3 superlattice structure with layer thicknesses of 0.5 nm/0.1 nm. Cross-plane transport properties were determined.
[c] Basal plane transport properties were determined.
[d] Accuracy of chemical analysis unclear.

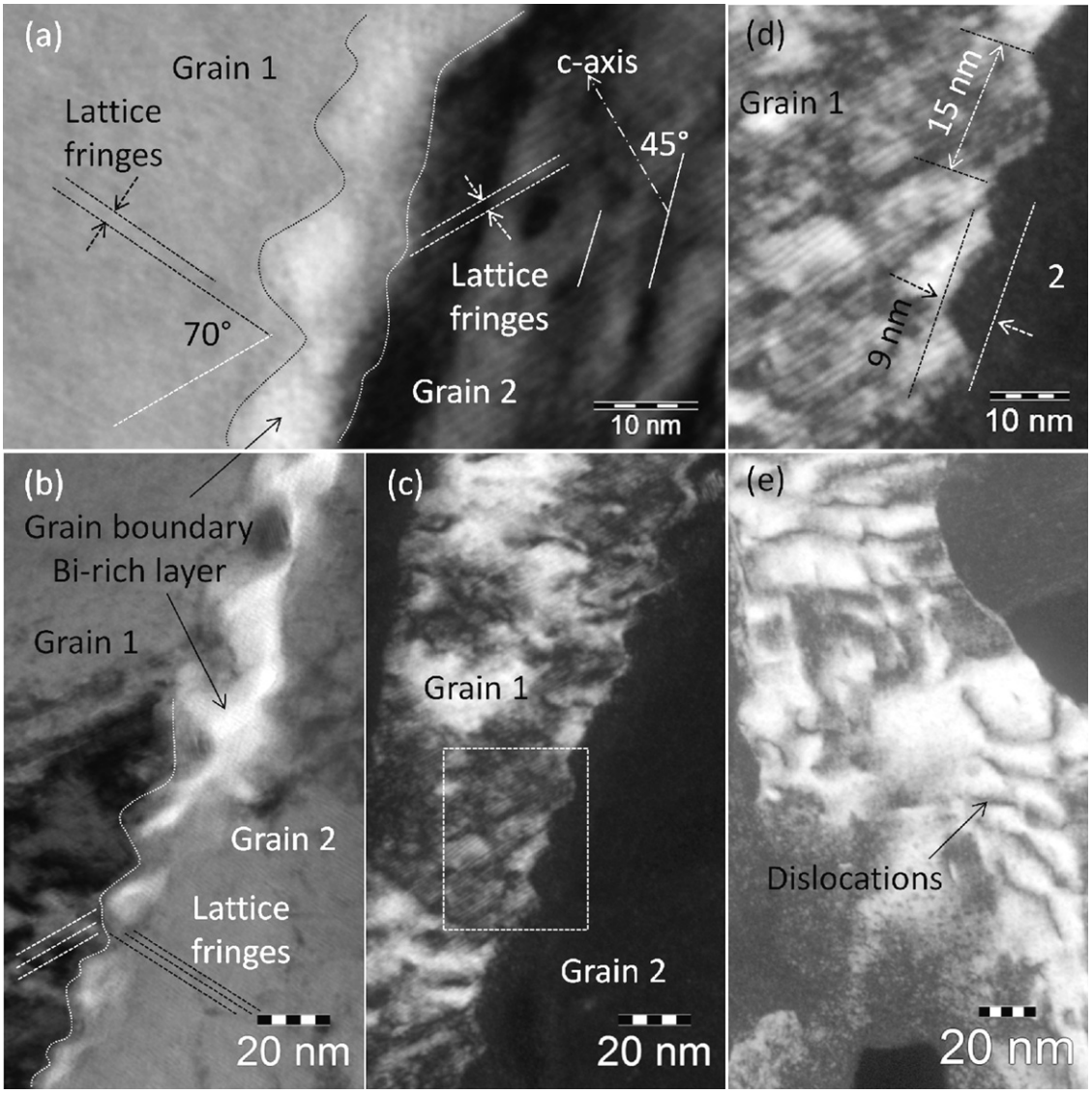

Fig. 10. TEM images acquired on grain boundaries in the annealed Bi_2Te_3 thin film deposited on a SiO_2 substrate (sample BT-S2): (a) High-resolution TEM image of adjacent grains separated by a grain boundary layer. (b) Bright-field and (c) dark-field TEM images of a facetted grain boundary. (d) Magnified image of selected region as indicated in (c). (e) Dark-field image of a grain with dislocations.

properties of Sb_2Te_3 as-grown films were close to that of annealed films.

In contrast to Sb_2Te_3 thin films, as-deposited Bi_2Te_3 films yielded metallic properties and XRD revealed $\{0\,0\,l\}$ as well as other $\{h\,k\,l\}$ reflections of the Bi_2Te_3 structure. More detailed TEM cross-section analysis is necessary to clarify the as-grown film structure.

4.2. Annealed films: transport properties, impact of annealing temperature and nanostructure

Nano-alloyed Sb_2Te_3 films revealed favorable transport properties with small charge carrier densities ($p = 2.6 \times 10^{19}\,cm^{-3}$) and thereby large thermopower ($S = 130\,\mu V\,K^{-1}$), being a factor of 1.6 larger compared to bulk materials (Table 5). Bi_2Te_3 films also revealed a small charge carrier density ($n = 2.7 \times 10^{19}\,cm^{-3}$) and moderate values of the thermopower ($S = -153\,\mu V\,K^{-1}$) (Table 5).

As compared to bulk, the Bi_2Te_3 and particularly Sb_2Te_3 nano-alloyed thin films revealed strikingly small charge carrier densities of about $2.7 \times 10^{19}\,cm^{-3}$. This yielded large absolute thermopowers of 130–150 $\mu V\,K^{-1}$ (Table 5). In the literature, Sb_2Te_3 and Bi_2Te_3 thin films grown by MBE and MOCVD were reported with similar small charge carrier densities (Table 5). As shown by Miller and Li [29], in Bi_2Te_3 based materials the density of charge carriers is determined by the density of antisite defects, being regulated by the temperature the materials were exposed to. Thin films are exposed to low substrate and annealing temperatures between 225 °C and 350 °C, whereas bulk materials are exposed to high congruent melting temperatures beyond 565 °C (Table 5). Therefore, particularly for Sb_2Te_3 thin films low charge carrier densities are related to low annealing temperatures. The reduced charge carrier densities found in thin films are a key factor for their transport properties and could partially be explained [30] by the antisite defect model of Miller and Li.

The charge carrier mobility is determined by the relaxation time and effective masses. For n-type Bi_2Te_3 the effective masses associated with the conduction band are by factor of 1.4 smaller as compared to the effective masses associated with the valence band of p-type Bi_2Te_3 [31,32]. Band structure calculations confirmed these experimental findings [33–35]. Therefore, larger charge carrier mobilities were expected for n-type Bi_2Te_3 thin films as compared to p-type Bi_2Te_3 bulk. However, charge carrier mobilities in Bi_2Te_3 thin films were significantly smaller than in Bi_2Te_3 bulk

(Table 5), the reason will be discussed below. Finally, note that the main scattering mechanism in Bi_2Te_3, Sb_2Te_3, and mixed crystals is assumed to be electron scattering by acoustic phonons [36–38].

The in-plane charge carrier mobilities of polycrystalline Sb_2Te_3 and Bi_2Te_3 thin films presented here differed significantly from mobilities in the basal plane of single-crystal bulk (Table 5). Note that high-energy XRD showed that in-plane transport properties measured here are to a large extent basal-plane properties, see below. The Sb_2Te_3 thin film yielded a surprisingly high mobility ($402\,cm^2\,V^{-1}\,s^{-1}$) as compared to single-crystal bulk ($365\,cm^2\,V^{-1}\,s^{-1}$) although it contained grain boundaries (Table 5). The grain size was 500 nm for Sb_2Te_3 as determined by TEM cross-section analysis.

In contrast, in *n*-type Bi_2Te_3 thin films the charge carrier mobility ($80\,cm^2\,V^{-1}\,s^{-1}$) was reduced by a factor of 6–8 as compared to *p*-type Bi_2Te_3 bulk materials (Table 5). In these films Bi-rich grain boundary phases (Fig. 9(b)) are assumed to severely reduce charge carrier mobilities. The Bi-rich phases are assumed to be insulating since they showed in TEM high-resolution images a poor crystallinity (Fig. 10(a)) and turned out to be oxidized as shown by EDX in the TEM. Also, the grain boundary phases formed continuous layers extended in growth direction. Therefore, they act as electron blocking layers for in-plane transport. In Sb_2Te_3 thin films no electron blocking grain boundary phases were detected which is reflected by a large charge carrier mobility.

Energy-filtered TEM allows to easily detect these secondary phases and was applied for the first time to our knowledge. In Bi_2Te_3 based nanostructured bulk [39] also secondary phases were identified. Within our own research efforts on Bi_2Te_3 based nanostructured bulk and on multilayer Bi–Sb–Te nanowires [40] chemical modulations could be imaged by energy-filtered TEM.

4.3. Annealed films: impact of texture on transport properties

For Bi_2Te_3 materials texture has a significant influence on the measured transport data due to the anisotropy of the transport properties. The texture in the annealed thin films was analyzed by high-energy XRD in transmission and grazing incidence geometry and by electron diffraction on TEM cross sections. Particularly, high-energy XRD yielded a complete insight into texture of the films and epitaxial relations to the substrate and, to our knowledge, was not shown before by any other groups [3–12].

For both substrates, SiO_2 and BaF_2, the *c* axis was found to be preferentially oriented. Particularly for Bi_2Te_3 thin films deposited on BaF_2 substrates high-energy XRD patterns acquired in grazing incidence orientation yielded a 30° tilt of the *c* axis from growth direction (Fig. 6(d)). For Sb_2Te_3 thin films the *c* axis was found to be almost parallel to the growth direction, orientation deviations were smaller than 10° (not shown here). In contrast to epitaxial MBE, nano-alloyed thin films yielded no epitaxial relations between thin film and BaF_2 substrates [4]. Summarizing the texture analysis, the texture and the transport properties were hardly affected by the choice of the substrate (Table 2). The average $\{0\,0\,l\}$ plane was found to be moderately tilted by up to 30° with respect to the substrate plane and, in an oversimplified picture, can be assumed to be even parallel to it. Therefore, the transport properties of the films are to a large extent basal plane transport data.

4.4. Nano-alloying versus epitaxial growth of Sb_2Te_3 and Bi_2Te_3 thin films

Thin film growth by nano-alloying competes with MOCVD [3] and epitaxial MBE [4]. In Table 5 transport properties obtained in this work and of films reported in the literature are compared. Taylor et al. also deposited Bi_2Te_3 films at room temperature and annealed them after deposition [17]. Venkatasubramanian et al. used the MOCVD technique for growth of Bi_2Te_3/Sb_2Te_3 superlattice structures with outstanding high thermoelectric figures of merit [3]. Huang et al. also succeeded in MBE growth of Sb_2Te_3 and Bi_2Te_3 thin films [6]. Finally, results of a previous MBE study of epitaxially grown Bi_2Te_3 thin films were included in Table 5 [4,5].

Specific issues of the film deposition are stoichiometry control, surface roughness introduced by the growth process, and the deposition rate. As discussed above, films grown by the nano-alloying approach and by MBE and MOCVD yielded similar charge carrier densities since they were exposed to similar maximum temperatures (Table 5).

The growth rate of nano-alloyed Sb_2Te_3 films (0.3 μm/h) was slightly smaller than for nano-alloyed Bi_2Te_3 films (0.4 μm/h) and for epitaxially MBE (0.4 μm/h) [4]. After annealing Sb_2Te_3 films revealed a surface roughness of 40 nm being a factor of 2 smaller as compared to Bi_2Te_3 films.

Among other Sb_2Te_3 based thin films and superlattices [3,6–9], nano-alloyed Sb_2Te_3 films yielded small charge carrier densities ($2.6\times10^{19}\,cm^{-3}$) and highest charge carrier mobilities ($402\,cm^2\,V^{-1}\,s^{-1}$), see Table 5. Particularly, the charge carrier mobilities in nano-alloyed thin films exceeded values observed in high-*ZT* Bi_2Te_3/Sb_2Te_3 superlattice structures grown by MOCVD by Venkatasubramanian et al. [3] (Table 5). Because small carrier densities were obtained in both, in nano-alloyed thin films presented here and high-*ZT* superlattice structures grown by MOCVD, it can be concluded that in superlattice structures besides quantum confinement and enhanced phonon scattering the point defect densities are a third crucial factor strongly affecting the thermoelectric properties.

Transport properties of Bi_2Te_3 films prepared by nano-alloying and epitaxial MBE [4] will be compared here (Table 5): (i) charge carrier densities were very close, *i.e.*, $2.7\times10^{19}\,cm^{-3}$ for nano-alloying and $3.3\times10^{19}\,cm^{-3}$ for epitaxially MBE. This indicates that the temperature the films were exposed to governs their point defect concentration and therefore their charge carrier density. (ii) Also, for epitaxial MBE only *n*-type Bi_2Te_3 films could be obtained, confirming that the point defect physics is similar and is governed by the temperature. (iii) The mobility of epitaxially grown films was found to be significantly higher, *i.e.*, $120\,cm^2\,V^{-1}\,s^{-1}$ for epitaxial films as compared to $80\,cm^2\,V^{-1}\,s^{-1}$ for the nano-alloyed films. The difference can be attributed to the texture and the Bi-rich grain boundary layers, which did not appear in epitaxially grown films [4]. (iv) Epitaxially grown films yielded a significantly larger thermopower of $-201\,\mu V\,K^{-1}$ as compared to $-153\,\mu V\,K^{-1}$ measured in nano-alloyed films. In summary nano-alloyed Bi_2Te_3 thin films compete with epitaxial Bi_2Te_3 films with respect to charge carrier density and thermopower but yielded severely smaller charge carrier mobilities.

5. Conclusions

Nano-alloying, *i.e.*, room-temperature MBE combined with subsequent annealing, yielded (i) stoichiometric thin films, (ii) an accurate and easy control of the Te content, (iii) a high-quality layer-by-layer growth, (iv) polycrystalline films with average grain sizes of 500 nm for the Sb_2Te_3 and 250 nm for the Bi_2Te_3 films, and (v) a texture with the basal plane of the grains being inclined by up to 30° with respect to the plane of the film. Microstructures and transport properties were very similar for BaF_2 and SiO_2 substrates. Thus nano-alloying could be a key technology for an industrial large-scale production of thin film devices. Nano-alloyed, *p*-type Sb_2Te_3 thin films were competitive with high-*ZT* *p*-type Bi_2Te_3/Sb_2Te_3 superlattices grown by MOCVD [3] due to their small charge carrier densities ($p=2.6\times10^{19}\,cm^{-3}$) and an outstanding charge carrier mobility ($\mu=402\,cm^2\,V^{-1}\,s^{-1}$). They also yielded a

large thermopower ($S = 130\,\mu V\,K^{-1}$) and thereby a large power factor ($S^2\sigma = 29\,\mu W\,cm^{-1}\,K^{-2}$) as compared to bulk. For Bi_2Te_3 thin films, nano-alloying competes with epitaxial MBE [4,5] due to a small charge carrier density ($n = 2.7 \times 10^{19}\,cm^{-3}$) and a moderate thermopower ($S = -153\,\mu V\,K^{-1}$). However, nano-alloyed Bi_2Te_3 thin films yielded a small power factor ($S^2\sigma = 8\,\mu W\,cm^{-1}\,K^{-2}$) due to a small charge carrier mobility ($\mu = 80\,cm^2\,V^{-1}\,s^{-1}$), Bi-rich blocking layers were identified as reason for the low charge carrier mobilities. A combination of advanced diffraction, imaging, and spectroscopy methods was applied for the first time on Bi_2Te_3 based thin films. High-energy X-ray diffraction, high-accuracy energy-dispersive X-ray spectroscopy, and energy-filtered TEM were of paramount importance to monitor texture, chemical composition, and grain boundary phases in order to interpret transport properties correctly.

Acknowledgements

The authors gratefully acknowledge financial support by the German Research Society DFG, priority programme 1386 "Nanostructured Thermoelectric Materials: Theory, Model Systems and Controlled Synthesis." R.P.H. and D.B. acknowledge the Advanced Photon Source for provision of synchrotron radiation beam time and the help of Dr. D. Robinson during data acquisition at 6-ID-D. R.P.H. acknowledges support from the Helmholtz–University Young Investigator Group "Lattice Dynamics in Emerging Functional Materials."

References

[1] D.M. Rowe, CRC Handbook of Thermoelectrics, CRC, Boca Raton, FL, 1995, Chapter 19.
[2] L.D. Hicks, M.S. Dresselhaus, Phys. Rev. B 47 (1993) 12727–12731.
[3] R. Venkatasubramanian, E. Siivola, T. Colpitts, B. O'Quinn, Nature (London) 413 (2001) 597–602.
[4] N. Peranio, O. Eibl, J. Nurnus, J. Appl. Phys. 100 (2006) 114306.
[5] D.M. Rowe, Thermoelectrics Handbook Macro to Nano, CRC Press, Boca Raton, FL, 2006, Chapter 48.3.6.
[6] B. Huang, C. Lawrence, A. Gross, G.-S. Hwang, N. Ghafouri, S.-W. Lee, H. Kim, C.-P. Li, C. Uher, K. Najafi, M. Kaviany, J. Appl. Phys. 104 (2008) 113710.
[7] L.W. da Silva, M. Kaviany, C. Uher, J. Appl. Phys. 97 (2005) 114903.
[8] L.M. Goncalves, P. Alpuim, G. Min, D.M. Rowe, C. Couto, J.H. Correia, Vacuum 82 (2008) 1499–1502.
[9] H. Zou, D.M. Rowe, S.G.K. Williams, Thin Solid Films 408 (2002) 270–274.
[10] H. Zou, D.M. Rowe, G. Min, J. Cryst. Growth 222 (2001) 82–87.
[11] L.M. Goncalves, C. Couto, P. Alpuim, A.G. Rolo, F. Völklein, J.H. Correia, Thin Solid Films 518 (2010) 2816–2821.
[12] E. Charles, E. Groubert, A. Boyer, J. Mater. Sci. Lett. 7 (1988) 575–577.
[13] G. Wang, L. Endicott, C. Uher, Sci. Adv. Mater. 3 (2011) 539–560.
[14] A. Mzerd, D. Sayah, G. Brun, J.C. Tedenac, A. Boyer, J. Mater. Sci. Lett. 14 (1995) 194–197.
[15] H. Böttner, A. Schubert, H. Kölbel, A. Gavrikov, A. Mahlke, J. Nurnus, Proceedings of the 23rd International Conference on Thermoelectrics (ICT 2004), Adelaide, Australia, 2004 (IEEE, Piscataway, NJ, 2004), Paper No. 9.
[16] D.C. Johnson, Curr. Opin. Solid State Mater. Sci. 3 (1998) 159–167.
[17] A. Taylor, C. Mortensen, R. Rostek, N. Nguyen, D.C. Johnson, J. Electron. Mater. 39 (2010) 1981–1986.
[18] D. Eyidi, D. Maier, O. Eibl, M. Westphal, Phys. Status Solidi A 187 (2001) 585–600.
[19] N. Peranio, O. Eibl, Phys. Status Solidi A 204 (2007) 3243–3255.
[20] S. Nakajima, J. Phys. Chem. Solids 24 (1963) 479–485.
[21] H. Hahn, W. Seemann, H.-L. Kohn, Z. Anorg. Allg. Chem. 369 (1969) 48–58.
[22] J. Nurnus, H. Böttner, H. Beyer, A. Lamprecht, Proceedings of the 18th International Conference on Thermoelectrics (ICT'99), Baltimore, MD, 1999 (IEEE, Piscataway, NJ, 1999), Catalog No. 99TH 8407, pp. 696–699.
[23] J.D. König, M. Winkler, S. Buller, W. Bensch, U. Schürmann, L. Kienle, H. Böttner, J. Electron. Mater. 40 (2011) 1266–1270.
[24] M. Winkler, D., Ebling, H. Böttner, L. Kirste, Proceedings of 8th European Conference on Thermoelectrics, Como, Italy, 2010, pp. 26–32.
[25] N. Peranio, O. Eibl, J. Appl. Phys. 103 (2008) 024314.
[26] G. Cliff, G.W. Lorimer, J. Microsc. 103 (1975) 203–207.
[27] T.L. Anderson, H.B. Krause, Acta Crystallogr. B 30 (1974) 1307–1310.
[28] N. Peranio, O. Eibl, Phys. Status Solidi A 206 (2009) 42–49.
[29] G.R. Miller, C.-Y. Li, J. Phys. Chem. Solids 26 (1965) 173–177.
[30] N. Peranio, M. Winkler, Z. Aabdin, J. König, H. Böttner, O. Eibl, Phys. Status Solidi A 209 (2012) 289–293.
[31] H. Köhler, Phys. Status Solidi B 74 (1976) 591–600.
[32] H. Köhler, Phys. Status Solidi B 73 (1976) 95–104.
[33] M. Kim, A.J. Freeman, C.G. Geller, Phys. Rev. B 72 (2005) 035205.
[34] G. Wang, T. Cagin, Phys. Rev. B 76 (2007) 075201.
[35] P. Larson, Phys. Rev. B 68 (2003) 155121.
[36] H.J. Goldsmid, Proc. Phys. Soc. Lond. 71 (1958) 633–646.
[37] L.R. Testardi, J.N. Bierly Jr., F.J. Donahoe, J. Phys. Chem. Solids 23 (1962) 1209–1217.
[38] M. Stordeur, M. Stölzer, H. Sobotta, V. Riede, Phys. Status Solidi B 150 (1988) 165–176.
[39] Y. Lan, B. Poudel, Y. Ma, D. Wang, M.S. Dresselhaus, G. Chen, Z. Ren, Nano Lett. 9 (2009) 1419–1422.
[40] N. Peranio, Z. Aabdin, W. Töllner, M. Winkler, J. König, O. Eibl, K. Nielsch, H. Böttner, MRS Proceedings 1329, 2011, mrss11-1329-i10-21 doi:10.1557/opl.2011.1238.